Arabian Journal of Chemistry (2023) **16**, 105002

King Saud University

Arabian Journal of Chemistry

www.ksu.edu.sa
www.sciencedirect.com

ORIGINAL ARTICLE

Solvent-dependent hypsochromic shift and ameliorative effects on breast cancer-induced bone metastases associated oxidative injury in rats

Khouloud Hchicha [a], Elena Cambiotti [b], Hmed Ben-Nasr [c], Daniel Chappard [d], Matti Haukka [e], Loredana Latterini [b], Salem Elkahoui [f,g], Arif J. Siddiqui [f,g], Mejdi Snoussi [f,g], Mohd Adnan [f,g,h], Houcine Naïli [a,*], Riadh Badraoui [f,g,i,*]

[a] *Laboratoire Physico-Chimie de l'Etat Solide, Département de Chimie, Faculté des Sciences de Sfax, B.P. 1171, 3000 Sfax, Université de Sfax, Tunisia*
[b] *Nano4Light-Lab, Dipartimento di Chimica, Biologia e Biotecnologie, Università degli Studi di Perugia, Via Elce di Sotto, 8, 06123 Perugia, Italy*
[c] *Laboratory of Pharmacology, Medicine Faculty of Sfax, University of Sfax, Sfax 3029, Tunisia*
[d] *Le Groupe d'Etudes Remodelage Osseux et bioMatériaux (GEROM)– LHEA, IRIS-IBS Institut de Biologie en Santé, CHU d'Angers, Université d'Angers, 49933 Angers Cedex, France*
[e] *Department of Chemistry, University of Jyväskylä, P.O. Box 35, FI-40014 Jyväskylä, Finland*
[f] *Laboratory of General Biology, Department of Biology, University of Ha'il, 81451 Ha'il, Saudi Arabia*
[g] *Molecular Diagnostic and Personalized Therapeutics Unit, University of Ha'il, Ha'il 81451, Saudi Arabia*
[h] *Department of Biochemistry, College of Medicine, University of Ha'il, 81451 Ha'il, Saudi Arabia*
[i] *Section of Histology–Cytology, Medicine Faculty of Tunis, University of Tunis El Manar, 1007 La Rabta, Tunis, Tunisia*

Received 10 February 2023; accepted 11 May 2023
Available online 18 May 2023

KEYWORDS

Imidazole-based complexes;
Hypsochromic shift;
Antioxidant potential;
Breast cancer;
Bone metastases;
Oxidative damage

Abstract A sulfate-bridged complex $[Cu(\mu_2\text{-}SO_4)(Im)_4]$ (**1**) was prepared and structurally characterized, where Im: imidazole. The X-ray structure analysis reveals that **1** crystallizes in the monoclinic system with space group C2/c. The octahedral coordination around the metal center is made up of four distinct imine nitrogen atoms in the equatorial plane, and two sulfate oxygen atoms occupying the axial sites. The covalent linkage between metals via the sulfate group, forming infinite 1D zigzag chains, ensures the entanglement of the structure. These chains, in turn, are further assembled into a 2D network through N—H···O hydrogen bonding. Thermal analyses underline the high thermal stability of our complex, which starts to decompose at 200 °C. The infrared spectrum confirms the results obtained from the crystallographic analysis. Optical studies reveal the presence of a hypsochromic effect noticed in the absorption and photoluminescence spectra. The

* Corresponding authors at: Laboratory of General Biology, Department of Biology, University of Ha'il, 81451 Ha'il, Saudi Arabia (R. Badraoui).
E-mail addresses: khouloud1907@ymail.com (K. Hchicha), elena.cambiotti@studenti.unipg.it (E. Cambiotti), daniel.chappard@univ-angers.fr (D. Chappard), matti.o.haukka@jyu.fi (M. Haukka), lore-dana.latterini@unipg.it (L. Latterini), s.elkahoui@uoh.edu.sa (S. Elkahoui), m.snoussi@uoh.edu.sa (M. Snoussi), houcine.naili@fss.rnu.tn (H. Naïli), riadh.badraoui@fmt.utm.tn, ri.badraoui@uoh.edu.sa (R. Badraoui).

https://doi.org/10.1016/j.arabjc.2023.105002

synthesized compound was found to reduce both oxidative injury and histopathological features, which are associated with skeletal metastases as a result of malignant Walker 256/B breast cancer cells.

1. Introduction

The self-assembly of metal-containing complexes is one of the most thriving areas of research in solid chemistry owing to their beguiling structural frameworks and their aptitude as functional materials in various fields such as catalysis (Yahyaoui et al., 2007; Naïli et al., 2013; Díaz-Requejo and Pérez, 2008; Kirillov et al., 2012), bioinorganic chemistry (Solomon et al., 2004; Henkel and Krebs, 2004; Gamez et al., 2001), and magnetochemistry (Sharples and Collison, 2014; Coronado and Day, 2004). The structure of those complexes can be designed based on the interaction of metal ions with organic ligands. In the self-assembly process, the duly selection of the metal ions, the structure of the organic ligands, the nature of counter anions, and the reaction conditions alter the formation of the final architecture. Although it is not yet possible to prepare fully predictable frameworks based on rational design, the appropriately selected organic ligand is of primordial importance in the adjustment of the topology of coordination frameworks. As stated in previous studies, N-containing ligands tend to evolve strong coordination bonds to metal ions materials (Abid Derbel et al., 2020; Sayer et al., 2021; Ben Salah et al., 2016).

Among N-containing ligands, imidazole is a flexible building block employed in the synthesis of numerous natural products, as well as an important substituent in a large variety of pharmacologically active compounds and therapeutic medicine (Derbel et al., 2022; Mhadhbi et al., 2023; Verma et al., 2013). Imidazole is a polar and ionizable aromatic component that may be used to optimize the solubility and bioavailability aspects of developed medicinal compounds (Adhikary et al., 2016). Therefore, a great number of research publications have been published on the production, antimicrobial, and anticancer characteristics of imidazole-derived copper(II)-complexes (Inci et al., 2021; Khan et al., 2020; Jiang et al., 2022; Kumar and Goel, 2022). Recent studies on transition metal complexes with imidazole moiety demonstrated that they limit tumor development by interacting with DNA (Adimule et al., 2021; Gerçek et al., 2022; Yasir Khan et al., 2022). Mercaptopurine, an imidazole-based anticancer medication, has been shown to treat leukemia by interfering with DNA synthesis (Rayati et al., 2017).

It is also well known that sulfate anions are attractive linkers for generating novel convoluted structures due to their ability to bind multiple metal sites. It can accommodate 16 bridging coordination modes that can bond 2, 3, 4, 5, 6, 8, or 10 metal ions, allowing for tremendous structural diversity (Papatriantafyllopoulou et al., 2008; Hfidhi et al., 2019; Hfidhi et al., 2021).

Recently, it has been reported that N-donor ligand 2-methylimidazole generates a dimeric sulfate-bridged structure by its reaction with copper(II) sulfate pentahydrate, which revealed compelling ameliorative effects on tumor osteolytic lesions in malignant Walker 256/B breast cancer-induced bone metastases in vivo and in vitro (Hchicha et al., 2021; Mhadhbi et al., 2022). Moreover, imidazole nucleus is inimitable and ubiquitous and it is well known to play a key role in living organisms. Its derivatives have been reported as potential therapeutic agents. They reduced proliferation and possessed metabolic and antioxidative activities (Sharma et al., 2016; Gallati et al., 2021).

Inspired by the above-mentioned facts, we report in this paper the synthesis, optical and for the first time the in vivo antioxidant and anticancer properties of a new sulfate-bridged Cu(II) promising complex. Its structure, which has been reported (Kumar et al., 2014), consists of $[Cu(\mu_2\text{-}SO_4)(Im)_4]$ units that are bridged by the sulfate group to form an infinite 1D coordination chain that is reinforced by the presence of hydrogen bonding between the organic ligand and the sulfate O atoms. The optical properties of the synthesized compound are explored in solutions, using media with different polarities. In an attempt to rationalize the antioxidant and anti-tumoral effects of the title complex, we used a rat model of breast cancer skeletal metastases (BCSM).

2. Material and methods

2.1. Materials

All chemicals used during this work were of analytical grade and were purchased from Sigma Aldrich. They were used as received without any further purification. All the solvents used in the synthesis were pure and obtained from chemical suppliers.

2.2. Synthesis process

Single crystals of **1** (Fig. 1) were successfully grown by the slow evaporation method at room temperature. Imidazole (0.27 g, 4 mmol) of was dissolved separately in 10 mL of methanol. Then, copper sulfate pentahydrate (0.25 g, 1 mmol) was added to the resulting solution under continuous stirring. An hour later, the homogenous solution was filtered using Whatman filter paper and kept in a dust-free environment for crystallization. Dark blue crystals appeared after a few days, filtered off and washed with methanol, then air-dried.

2.3. Physical measurements

Infrared measurements were recorded at room temperature with a Bruker Optics, Vertex70 FT-IRspectrophotometer, using KBr pellets, in the range of 400–4000 cm^{-1}.

For investigation of the thermal properties of **1**, a thermogravimetric (TG) analysis and a differential thermal analysis (DTA) were conducted using a simultaneous TGA/DTA thermal analyzer NETZSCH STA 449C TGA/DTA system with a UMX1 balance from room temperature to 1000 °C under airflow (100 mL/min) at a constant rate of 10 °C/min. The measurement of differential scanning calorimetry (DSC) was performed on a NETZSCH DSC 200 F3 instrument in the temperature range of 35–400 °C.

UV–Vis spectra are collected through a Cary 8454 UV–Vis Diode Array spectrophotometer using a 1 cm path length quartz cuvette. Luminescence measurements are carried out using an Edinburgh FS5 spectrofluorometer.

2.4. X-ray data collection

A suitable crystal of **1** was selected under an optical microscope and glued to thin glass fiber. The intensity data of the

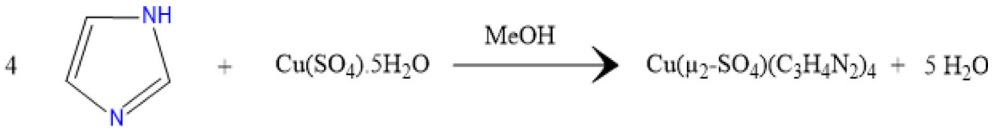

Fig. 1 Reaction scheme of the synthesis of **1**.

crystal were recorded on an Oxford Gemini S diffractometer. The diffractometer was operated with Mo-Kα radiation (λ = 0.71073 Å). A multi-scan and empirical absorption correction were applied with the SADABS program (Sheldrick, 1996). The structure was solved using the intrinsic phasing method and refined against full-matrix least-squares methods F2 using SHELXT, and SHELXL2018/3 software. The NH hydrogen atoms were located from the difference Fourier map and refined isotropically. Other hydrogen atoms were positioned geometrically and constrained to ride on their parent at-oms, with C—H = 0.95–0.98 Å, N—H = 0.91 Å, and Uiso = 1.2–1.5 Ueq (parent atom). The highest peak is located 0.79 Å from atom O1 and the deepest hole is located 0.61 Å from atom O_2. The molecular graphics were designed using the DIAMOND program. A summary of the crystal data, experimental details, and refinement results is compiled in Table 1. CCDC 2158907 contains the supplementary crystallographic data for this paper. These data can be obtained free of charge from The Cambridge Crystallographic Data Centre via https://www.ccdc.cam.ac.uk/structures.

Table 1 Crystallographic and structure refinement data for **1**.

Structural parameter	Compound (1)
Empirical formula	$C_{12}H_{16}CuN_8O_4S$
Formula weight (g.mol^{-1})	431.93
Temperature (K)	235(2) K
Crystal system	Monoclinic
Space group	*C*2/*c*
a (Å)	9.2045(2)
b (Å)	17.6322(4)
c (Å)	10.4835(2)
β (°)	93.289(2)
Volume (Å^3)	1698.62(6)
Z	4
ρ_{cal} (mg.m^{-3})	1.689
Absorption correction	Semi-empirical from equivalents
Crystal size (mm^3)	0.140 × 0.070 × 0.060
Crystal color	Blue
μ (mm^{-1})	1.447
hkl range	$-12 \le h \le 13$ $-25 \le k \le 25$ $-14 \le l \le 11$
No. of reflection collected	8181
No. of independent reflection	3823
F (000)	884
R1[a] ($I \ge 2\sigma$)	0.0467
wR2[b] ($I \ge 2\sigma$)	0.0996
GooF	1.046
Transmission factors	Tmin = 0.87232, Tmax = 1.00000
Largest difference map hole (eÅ^{-3})	Δρmin = −0.353; Δρmax = 0.912

[a] $R1 = \Sigma||F_o| - |F_c||/\Sigma|F_o|$.
[b] $wR_2 = \{\Sigma[w(F_o^2 - F_c^2)^2]/\Sigma[w(F_o^2)^2]\}^{1/2}$.

2.5. Biological activities: Antioxidant and anti-tumoral effects

2.5.1. Animal farming and experimental procedure

Mature *Wistar* male rats (n = 24) were farmed under standard animal housing conditions (24 °C, 50% humidity, and 12/12 h light/dark cycles). The experimental BCSM was induced via an intra-femoral inoculation model using malignant Walker 256/B breast cancer cells as previously described (Badraoui et al., 2014; Nyangoga et al., 2010; Badraoui et al., 2020). Previous studies indicated that it is a very reproducible rat model of BCSM (Nyangoga et al., 2010; Badraoui et al., 2022; Hchicha et al., 2021). The rats were randomly divided into four groups:

- Six rats were sham-operated under general anesthesia (ketamine and xylazine) and served as a control group (CTRL).
- Six rats received intra-femoral inoculation of 5 × 10^4 Walker 256/B cells under general anesthesia and served as the W256 group.
- Six rats were sham-operated under general anesthesia and given three intramuscular injections of the synthesized complex (36 mg kg^{-1}) based on one injection/week. These rats served as **1** group.
- Six rats received intra-femoral inoculation of 5 × 10^4 Walker 256/B cells under general anesthesia and were given three intra-muscular injections of the synthesized complex (36 mg kg^{-1}) as prescribed above. These rats served as the W256 + **1** group.

Twenty days after surgery, all rats were euthanized. Operated femurs and bone morrow of the tumor vicinity were collected for either histological or biochemical analyses as recently reported (Badraoui et al., 2014; Nyangoga et al., 2010; Badraoui et al., 2020). Animal housing and experimental procedures were carried out using the Guidelines for Care and Use of Laboratory Animals of Sfax University and approved by the local Ethical Committee (12/ES/15). The main reasons behind the selected dose of **1** is bibliography and similar compounds as reported in previous studies, including those realized in our research laboratory.

2.5.2. Antioxidant potential assay

The oxidative injury parameters were performed in the bone morrow metastatic environment of the different experimental groups as previously reported (Mzid et al., 2017; Badraoui et al., 2007). The pro-oxidant parameters include thiobarbituric acid reactive substances (TBARS) and advanced oxidation of protein products (AOPP). TBARS level was assessed spectrophotometrically following the method of Draper and Hadley (Draper and Hadley, 1990). The absorbance was measured at 532 nm. AOPP levels were assessed spectrophotometrically using the method previously reported by Kayali (Kayali et al., 2006). The absorption of the reaction mixture

was measured at 340 nm. The antioxidant parameters include the assessment of superoxide dismutase (SOD), catalase (CAT), and glutathione peroxidase (GPX) activities. SOD, CAT, and GPX activities were assessed spectrophotometrically using the methods of Beauchamp and Fridovich (1971), Aebi (1984), Flohé and Günzler (1984), respectively. The protein quantification in both tissues (bone morrow and erythrocytes) was performed as previously described by Waterborg (2009) using bovine serum albumin.

2.5.3. Standard histological assay

The operated femurs of the different experimental groups were removed and processed for standard histological analyses following the decalcification procedure. The bone samples were embedded in paraffin and then cut into 4–5 µm. The obtained sections were stained with hematoxylin-eosin (HE) and examined under an optic Leica® microscope (Nyangoga et al., 2010; Badraoui et al., 2020). The histopathological examination was performed blindly.

2.5.4. Statistical analyses

Biological data are expressed as mean ± standard error of the mean (SEM). The statistical analyses included a one-way analysis of variance (ANOVA) followed by the Newman–Keuls post hoc test after checking the normal distribution. The statistical analyses were performed using the GraphPad software package (SPSS Inc., Chicago, IL, USA). The statistically significant difference was considered whenever $p < 0.05$.

3. Results and discussion

3.1. Infrared spectroscopy

The strong band at 3101 cm^{-1} is assigned to ν(NH), indicating the presence of neutral (Im) ligands in **1** (Tatara et al., 2003) (Fig. 2A). The [2800–3100] cm^{-1} spectral range shows relatively weak bands corresponding to the stretching vibration of (C—H) in the imidazole ring. A band at 1544 cm^{-1} indicates the (C═N) vibration, shifted toward lower wavenumbers, indicating the binding of imidazole to copper through the pyridine-type nitrogen atom. Additional stretching and deformation vibration modes of (C—C) and (C—N) appear in the [1400–1600] cm^{-1} and 600–900 cm^{-1} spectral range, respectively. Additionally, the ν_1 of the (—SO_4) group appears at 943 cm^{-1}, while ν_2 appears between 450 and 480 cm^{-1}. The split of the ν_3 (1062, 1112, 1155 cm^{-1}) and ν_4 (642, 608, 594 cm^{-1}) into three bands each evidence the bidentate coordination mode of the sulfate group (Krushna et al., 1977).

3.2. Thermal behavior

According to the TGA/DTA curve (Fig. 2B), complex **1** is thermally stable up to 200 °C proving the absence of any lattice or coordinated water/methanol molecules and the high thermal stability of our complex. Moreover, it can be handled safely in ambient air conditions. Even at high humidity, no hygroscopic phenomena are detected, which is of primordial importance for producing stable devices. The thermal evolution under air takes place in two consecutive stages. The first major weight loss of the material occurs between the temperatures of 200 °C and 400 °C, accompanied by an endothermic peak at 280 °C on the DTA thermogram. This mass loss corresponds to the oxidative degradation of four organic molecules. This coincides with a sharp endothermic peak at 285 °C on the DSC curve (Fig. 2C). In the second step, between the temperatures of 420 °C and 650 °C, an additional weight loss of 27% indicates the decomposition of the sulfate group (27.6% theoretical). In this temperature range, a shoulder exothermic peak appears on the DTA thermo-gram indicating that the remained phase absorbs energy to break the bonds between atoms leading to material decomposition.

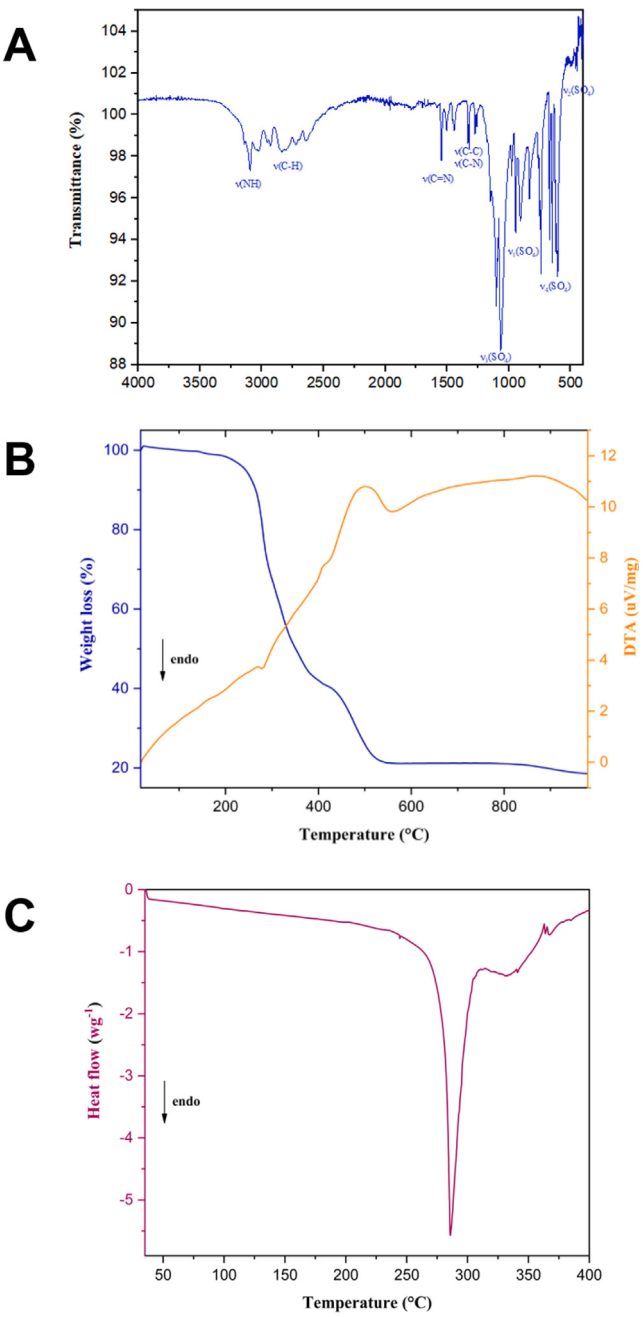

Fig. 2 (A): The Infrared spectra of **1** (KBr pellet). (B): Simultaneous TG-DTA curves for the decomposition of **1**. (C): DSC curve of **1**.

The final residue of the last step is expected to be copper oxide (CuO) as a final product.

3.3. Crystal structure determination

The title compound crystallizes in the monoclinic system with the centrosymmetric space group C2/c. Bond lengths (Å), bond angles (°), and torsion angles (°) are gathered in Table 2.

As shown in Fig. 3, the coordination geometry around the copper is well described as Jahn–Teller distorted octahedral with four short bonds in the equatorial plan formed by the imine nitrogen atoms, from four distinct (Im) molecules (Cu(1)—N(1) 2.0011(17) Å; Cu(1)—N(3) 2.0217(18) Å). While the axial sites are occupied by the two oxygen atoms from two sulfates anions, with a Cu—O bond length (2.557 (26) Å) that is significantly longer than the equatorial ones.

To determine the degree of structural distortion within [Cu(μ_2-SO_4)$(Im)_4$] octahedron, we define the distortion index (Δ) (Ben Ali et al., 2020):

$$\Delta = \frac{1}{6}\sum_{i=1}^{6}\frac{(d_i - \bar{d})^2}{\bar{d}}$$

in which d_i is the average Cu—N/O bond length and $\bar{d}$ are the distances of the six individual Cu—N/O bonds.

The herein obtained Δ value of 1.493×10^{-2} describes the environment around the metal ion to be a highly distorted octahedron.

The crystal structure of **1** exhibits a one-dimensional (1D) zigzag chain structure (Fig. 4A) built up by metal centers, SO_4^{2-} ions, and the *Im* ligands. The way of coordination of sulfate is a captivating structural aspect of this complex. **1** contains two bidentate bridging sulfate groups. Each of them stitches the adjacent copper ions in η^1:η^1:μ_2 or 2.1100 connectivity), giving rise to an infinite chain [—Cu(Im)$_4$—O—S(O_2)—O]$_n$ running along the *c*-axis.

A convoluted network of hydrogen bonds upholds the concatenation of the different subunits in the crystal. A crystal packing diagram depicting the different hydrogen bonding is shown in Fig. 4B and selected bond distances and angles are enumerated in Table 3.

3.4. Optical properties

The sample is investigated in solutions, using media with different polarities; the optical and luminescence properties of **1** are examined in H_2O, DMSO, and four mixtures with different H_2O:DMSO ratios (Table 4) (Maryott and Smith, 1951).

Table 2 Selected bond geometries (Å/°) of 1.

S(1)—O(1)$^{\#2}$	1.4480(18)	Cu1—O1	2.577(26)
S(1)—O(1)	1.4480(18)	O(1)$^{\#2}$—S(1)—O(1)	114.4(2)
S(1)—O(2)	1.4669(19)	O(1)$^{\#2}$—S(1)—O(2)	108.69(13)
S(1)—O(2)$^{\#2}$	1.4669(19)	O(1)—S(1)—O(2)	108.65(12)
Cu(1)—N(1)	2.0011(17)	O(1)$^{\#2}$—S(1)—O(2)$^{\#2}$	108.65(12)
Cu(1)—N(1)$^{\#1}$	2.0012(17)	O(1)—S(1)—O(2)$^{\#2}$	108.69(14)
Cu(1)—N(3)$^{\#1}$	2.0217(18)	O(2)—S(1)—O(2)$^{\#2}$	107.5(2)
Cu(1)—N(3)	2.0218(18)	N(3)$^{\#1}$—Cu(1)—N(3)	180.00(5)

Symmetry transformations used to generate equivalent atoms:
$^{\#1}$ −x + 3/2, −y + 1/2, −z + 1.
$^{\#2}$ −x + 2, y, −z + 3/2.

The comparison of the band profile shows (Fig. 5) that the UV band is not remarkably affected by the medium polarity (Fig. 6a) although the measurements have a reduced accuracy for the absorption contribution of DMSO. On the other hand, the Vis-NIR band (Fig. 6b) is clearly influenced by the medium properties; by increasing the medium polarity the absorption maximum exhibits a hypsochromic shift of 85 nm (Fig. 6b).

The hypsochromic shift was also observed in photoluminescence (PL) analysis (Fig. 7). Moreover, the changes observed on the luminescence maximum occurs with modification of the band profile. In DMSO the PL spectrum has a structured shape with the two main maxima at 414 and 450 nm and an important shoulder at 380 nm; in water, the PL spectrum has a structureless profile centered at 389 nm. By modifying the H_2O:DMSO ratio, the emission band assumes both characteristic signals of two neat solvents. This behavior may indicate the presence of different emitting states.

3.4.1. Biological activities: Antioxidant and anti-tumoral effects

First of all, it has been reported by the daily checking that the rats with BCSM, as inoculated with malignant Walker 256/B cells (W256 and W256 + **1** groups), showed highly depressive symptoms similar to the previous reports (Badraoui et al., 2009, 2022; Hchicha et al., 2021). The histopathological data are reported in Fig. 8. Overall, our results showed that Walker 256/B cells induced tumor osteolysis below the growth plate per comparison to the CTRL group. The osteolysis concerned both cancellous and cortical bone. Nevertheless, the prominent loss was noticed in the secondary spongiosa as evidenced by disorganized morphology associated with disconnected and reduced trabeculae. This confirms the reproducibility of this murine model of malignant Walker 256/B breast cancer-induced bone metastases (Badraoui et al., 2009, 2020; Hchicha et al., 2021). While **1** given alone was not associated with any toxic and/or histopathological features, it showed significant alleviative effects in the femur morphology and its trabecular network in the group W256 + **1** once compared with W256/B. These results may highlight the potential ameliorative effects of copper (II). Our results corroborated previous studies, which confirmed the therapeutic claims of similar compounds, particularly against cancerous diseases. It includes those realized on a murine model of bone metastasis using sulfate-bridged binuclear copper complex (Hchicha et al., 2021) or natural compounds (Badraoui et al., 2009, 2014, 2022).

As represented in Table 5, the assessment of oxidative stress revealed that malignant Walker 256/B cells increased both TBARS and AOPP levels (1.92 vs. 4.35 and 0.92 vs. 3.21, respectively) in the metastatic microenvironment when compared with CTRL. Bone metastases as induced by these cells were also associated with depletion of antioxidant enzymes, particularly SOD and GPX for which the differences were statistically significant (23.66 vs. 14.34 and 3.48 vs. 2.04, respectively). This proves that cancerous diseases are generally accompanied by oxidative injury (Badraoui et al., 2009, 2014). The synthesized and characterized compound was found to prevent the antioxidant enzymatic depletions and lowered both levels of lipid and protein oxidation (TBARS and AOPP). Taken together, the biological activity assessment revealed a potential antitumor effect of the synthesized compound through alleviation of Walker 256/B induced tumor

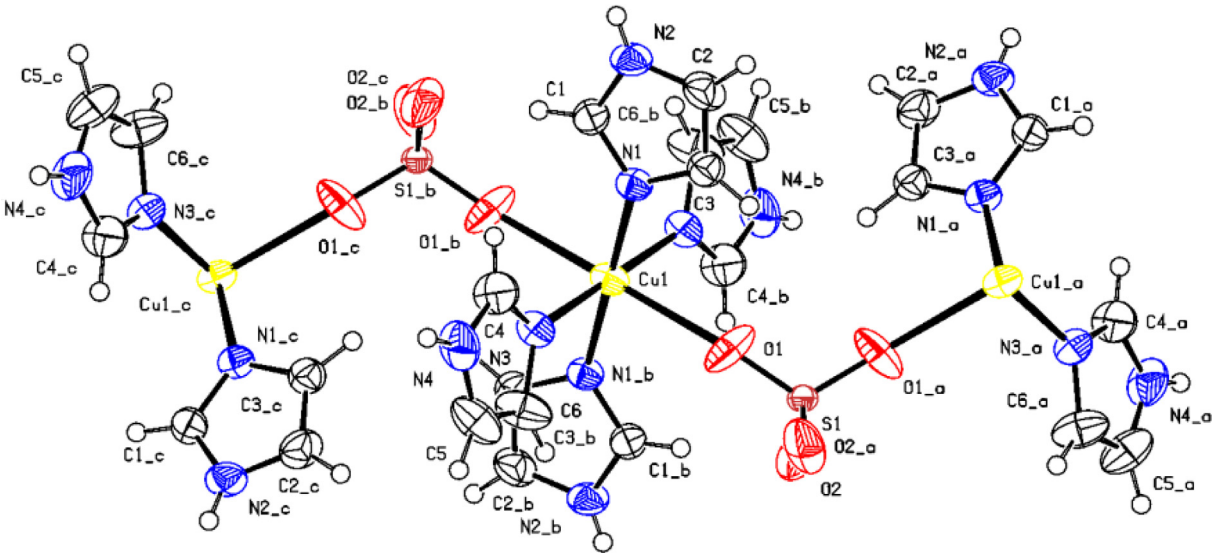

Fig. 3 ORTEP (50 % probability level) of the asymmetric unit of the molecular structure of **1** together with the atom numbering scheme. H atoms labels have been omitted for clarity.

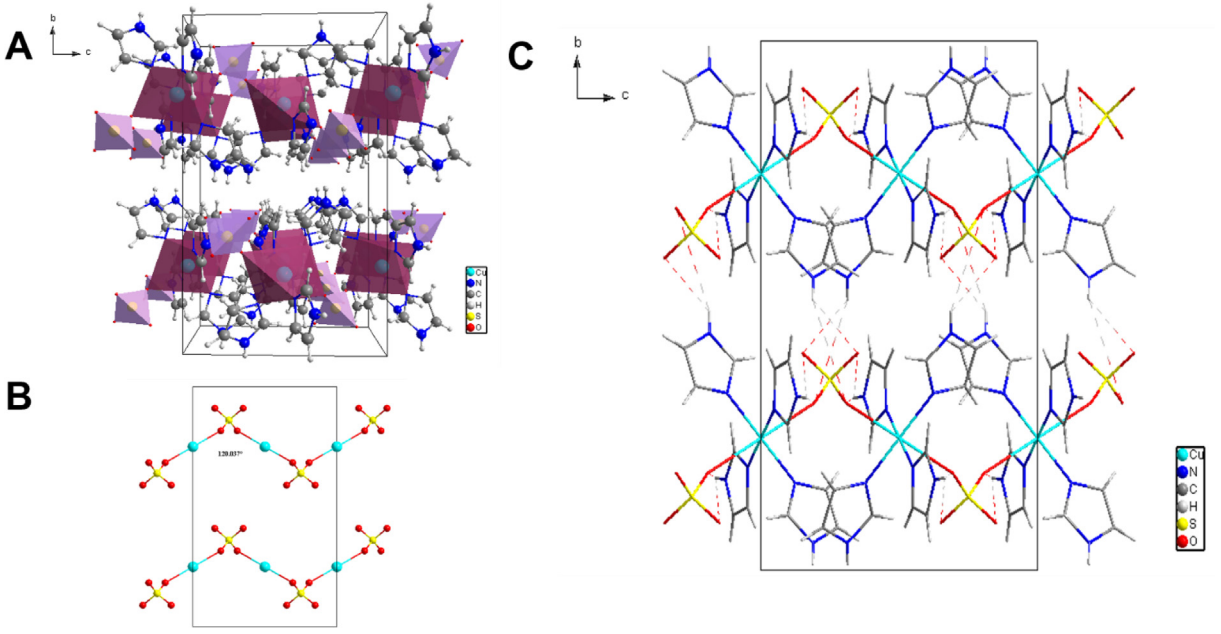

Fig. 4 (A) Packing of **1** along the crystallographic a-axis. (B) The sulfate-bridged zigzag chain viewed along c-axis. (C) Hydrogen bond network shown along the a-axis.

Table 3 Hydrogen bonds properties (Å/°) for 1.

D—H···A	*d*(D—H)	*d*(H···A)	*d*(D···A)	∠D—H···A
N(2)—H(2)···O(2)[#3]	0.76(3)	1.95(3)	2.703(3)	169(3)

Symmetry transformations used to generate equivalent atoms:
[#3] x − 1/2, y + 1/2, z.

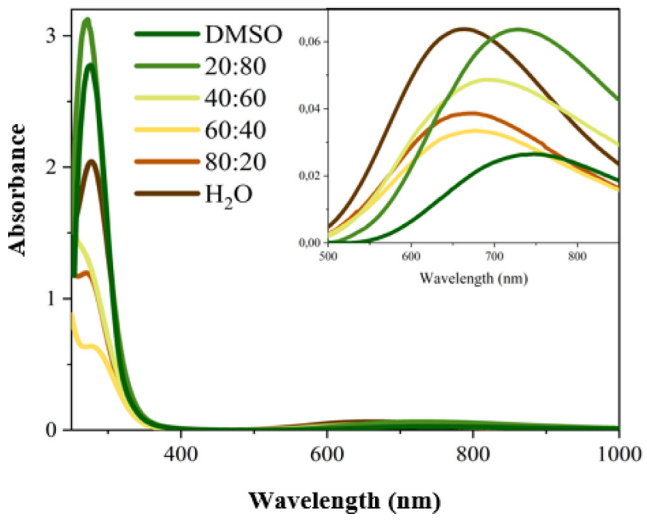

Fig. 5 Absorption spectra of the sample **1** in different media.

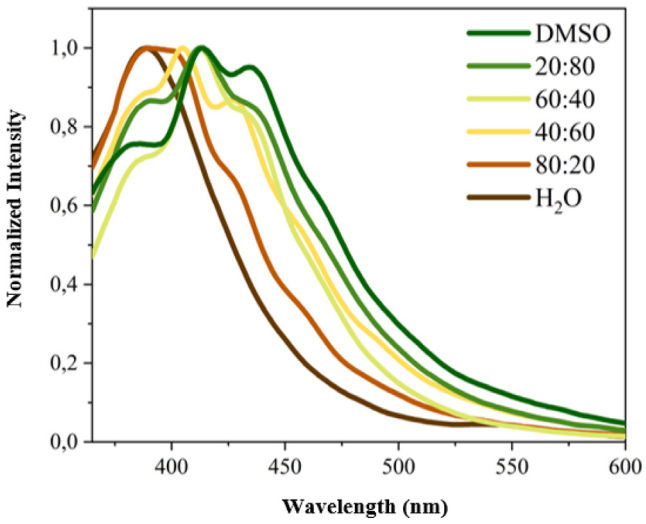

Fig. 7 Normalized PL spectra of **1** as function of medium polarity.

Table 4 The values of molar attenuation coefficient in different media.

Medium	ε
H_2O	80.1
H_2O:DMSO = 80:20	73.4
H_2O:DMSO = 60:40	66.7
H_2O:DMSO = 40:60	60.1
H_2O:DMSO = 20:80	53.4
DMSO	46.7

In general, the absorption spectra in different solutions (Fig. 8) display the first band in the UV and broadband at higher wavelengths.

osteolysis. These results may be the cause and/or the consequence of the potential antioxidative and/or anti-tumoral effects of **1**. Several similar synthesized or extracted compounds possessed such biological properties, which make them suitable candidates for drug design and development (Badraoui et al., 2009, 2014, 2022). Assessment of the druggability and pharmacokinetics would certainly confirm such interesting results.

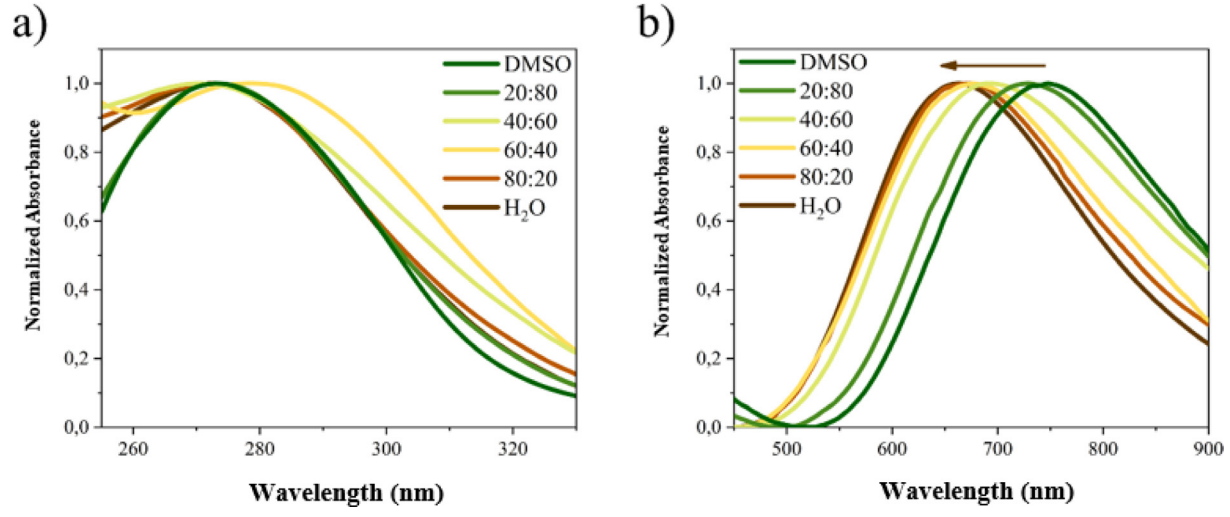

Fig. 6 Normalized absorption spectra of **1** in different media in UV (a) and NIR (b) region.

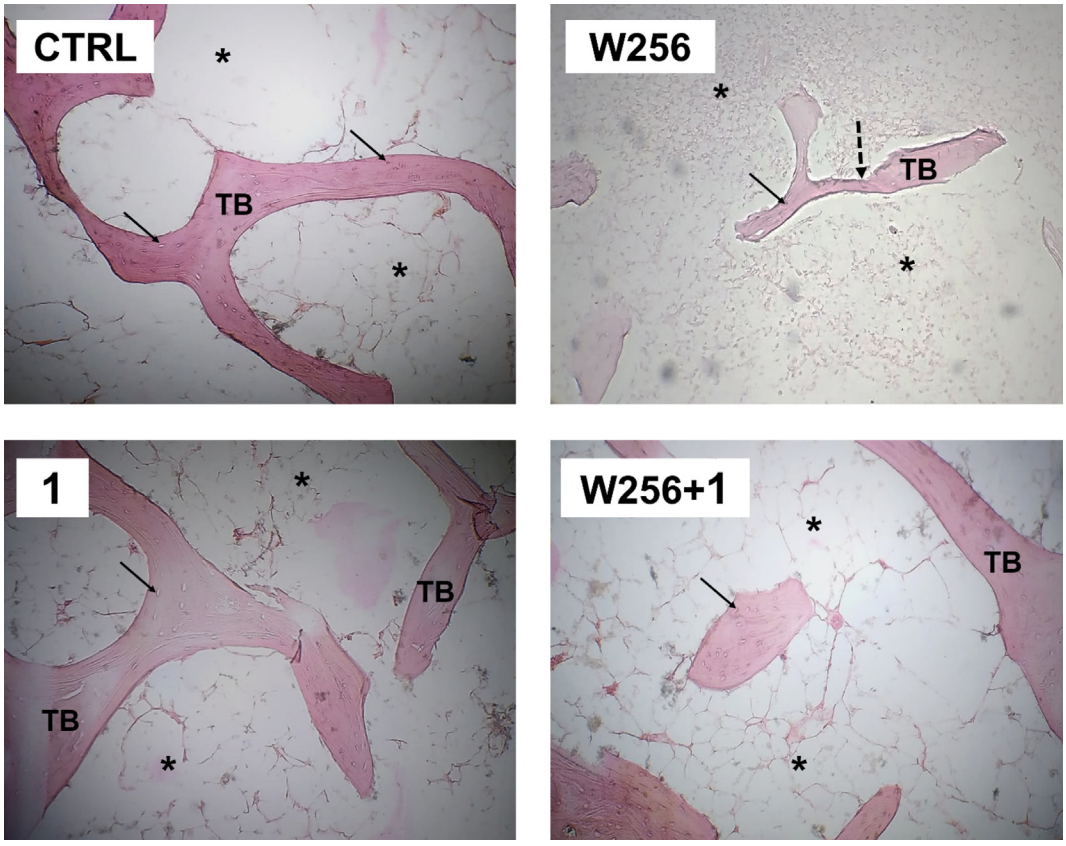

Fig. 8 Bone histological micrograph of CTRL (A), W256 (B), **1**(C), and W256 + **1**(D) groups (magnification × 200). Walker 256/B breast cancer cells were intrafemoral inoculated and rats were euthanized 20 days after surgery. Note the advanced tumor osteolytic lesions (dotted arrow) and the trabeculae thinning in W256 and W256 + **1** groups per comparison with CTRL. Note also the less prominent tumor osteolytic lesions in the W256 + **1** group once compared with W256. TB: trabecular bone; Asterisks: intertrabecular spaces, which are occupied by hematopoietic lineage, adipocytes, and Walker 256/B cells (if any); Arrow: Osteocytes.

Table 5 Pro-oxidant and antioxidant levels in the metastatic bone morrow environment of the different experimental groups CTRL, W256, **1,** and W256 + **1**.

Entry (unit)	Group			
	CTRL	**W256**	**1**	**W256 + 1**
Pro-oxidants				
TBARS (nmoles/mg protein)	1.92 ± 0.08	4.35 ± 0.12*	1.87 ± 0.07	3.22 ± 0.13*#
AOPP (nmoles/mg protein)	0.92 ± 0.04	3.21 ± 0.11*	0.96 ± 0.04	2.41 ± 0.08*#
Antioxidants				
SOD (Units/mg protein)	23.66 ± 0.86	14.34 ± 0.72*	22.84 ± 1.03	16.42 ± 0.75*
CAT (µmoles/min/mg protein)	17.43 ± 0.67	15.66 ± 1.02	18.66 ± 0.75	16.66 ± 0.83
GPX (µmoles/min/mg protein)	3.48 ± 0.45	2.04 ± 0.21*	3.36 ± 0.62	2.87 ± 0.54*#

Each data represents the mean ± SEM.
* $p < 0.05$ vs. CTRL group.
# $p < 0.05$ vs. W256 group using ANOVA followed by Newman–Keuls *post hoc* test.

4. Conclusion

The reaction of copper sulfate pentahydrate with imidazole in methanol was found to give complex **1**. The structure of the synthesized crystal was ascertained by single-crystal X-ray diffraction. The results unveil that the units of our complex self-assemble in μ_2-SO_4 bridged 1D infinite chains, which are further involved in hydrogen bonding. The metal ion is hexacoordinated by four N atoms from four *Im* ligands, and two O atoms from two sulfate groups leading to a distorted octahedral geometry. Thermal analyses highlighted the high thermal stability of our complex, and in complementarity by IR results support the results collected from single-crystal X-ray diffraction. A hypsochromic shift was detected in the absorption and photoluminescence spectra. The biochemical and histological studies suggested that **1** is expected to be an important complex for further analyses and development of both anti-oxidant and antitumoral drugs. The effect was proven in a pre-clinical experimental study in BCSM rats as induced by malignant Walker 256/B cells.

CRediT authorship contribution statement

Khouloud Hchicha: Conceptualization, Data curation, Methodology, Software, Writing – original draft. **Elena Cambiotti:** Data curation, Investigation, Methodology, Writing – original draft. **Hmed Ben-Nasr:** Formal analysis, Validation. **Daniel Chappard:** Investigation, Validation, Visualization. **Matti Haukka:** Data curation, Investigation, Validation. **Loredana Latterini:** Methodology, Validation. **Salem Elkahoui:** Formal analysis, Visualization. **Arif J. Siddiqui:** . **Mejdi Snoussi:** . **Mohd Adnan:** Formal analysis, Visualization. **Houcine Naïli:** Conceptualization, Data curation, Formal analysis, Supervision, Validation, Visualization, Writing – review & editing. **Riadh Badraoui:** Conceptualization, Data curation, Investigation, Methodology, Software, Project administration, Validation, Writing – original draft, Writing – review & editing.

Declaration of Competing Interest

The authors declare that they have no known competing financial interests or personal relationships that could have appeared to influence the work reported in this paper.

Acknowledgments

This research has been funded by Scientific Research Deanship at the University of Ha'il - Saudi Arabia through project number MDR-22 011.

References

Abid Derbel, M., Turnbull, M.M., Naïli, H., Rekik, W., 2020. A new mixed halide 2D hybrid perovskite: Structural, thermal, optic and magnetic properties. Polyhedron 175,. https://doi.org/10.1016/j.poly.2019.114220 114220.

Adhikary, J., Das, B., Chatterjee, S., Dash, S.K., Chattopadhyay, S., Roy, S., Chen, J.W., Chattopadhyay, T., 2016. Ag/CuO nanoparticles prepared from a novel trinuclear compound $[Cu(Imdz)_4(Ag(CN)_2)_2]$ (Imdz = imidazole) by a pyrolysis display excellent antimicrobial activity. J. Mol. Struct. 1113, 9–17. https://doi.org/10.1016/J.MOLSTRUC.2016.02.029.

Adimule, V., Yallur, B.C., Kamat, V., Krishna, P.M., 2021. Characterization studies of novel series of cobalt (II), nickel (II) and copper (II) complexes: DNA binding and antibacterial activity. J. Pharm. Investig. 51, 347–359. https://doi.org/10.1007/s40005-021-00524-0.

Aebi, H., 1984. Catalase in vitro. Meth. Enzymol. 105, 121–126. https://doi.org/10.1016/S0076-6879(84)05016-3.

Badraoui, R., Blouin, S., Moreau, M.F., Gallois, Y., Rebai, T., Sahnoun, Z., Baslé, M., Chappard, D., 2009. Effect of alpha tocopherol acetate in Walker 256/B cells-induced oxidative damage in a rat model of breast cancer skeletal metastases. J. Inorg. Nucl. Chem. 182, 98–105. https://doi.org/10.1016/J.CBI.2009.09.010.

Badraoui, R., Ben-Nasr, H., Amamou, S., El-May, M.V., Rebai, T., 2014. Walker 256/B malignant breast cancer cells disrupt osteoclast cytomorphometry and activity in rats: Modulation by α-tocopherol acetate. Pathol. Res. Pract. 210, 135–141. https://doi.org/10.1016/J.PRP.2013.11.002.

Badraoui, R., Boubakri, M., Bedbabiss, M., Ben-Nasr, H., Rebai, T., 2014. Walker 256/B malignant breast cancer cells improve femur angioarchitecture and disrupt hematological parameters in a rat model of tumor osteolysis. Tumor Biol 35, 3663–3670.

Badraoui, R., Rebai, T., Elkahoui, S., Alreshidi, M., Veettil, V.N., Noumi, E., Al-Motair, K.A., Aouadi, K., Kadri, A., De Feo, V., Snoussi, M., 2020. Allium subhirsutum L. as a Potential Source of Antioxidant and Anticancer Bioactive Molecules: HR-LCMS Phytochemical Profiling, In Vitro and In Vivo Pharmacological Study. Antioxidants 9, 1003. https://doi.org/10.3390/ANTIOX9101003.

Badraoui, R., Saeed, M., Bouali, N., Hamadou, W.S., Elkahoui, S., Alam, M.J., Siddiqui, A.J., Adnan, M., Saoudi, M., Rebai, T., 2022. Expression Profiling of Selected Immune Genes and Trabecular Microarchitecture in Breast Cancer Skeletal Metastases Model: Effect of α–Tocopherol Acetate Supplementation. Calcif. Tissue Int. 1, 1–14. https://doi.org/10.1007/S00223-021-00931-3/FIGURES/6.

Badraoui, R., Sahnoun, Z., Abdelmoula, N.B., Hakim, A., Fki, M., Rebaï, T., 2007. May antioxidants status depletion by Tetradifon induce secondary genotoxicity in female Wistar rats via oxidative stress? Pestic. Biochem. Physiol. 88 (2), 149–155.

Beauchamp, C., Fridovich, I., 1971. Superoxide dismutase: Improved assays and an assay applicable to acrylamide gels. Anal. Biochem. 44, 276–287. https://doi.org/10.1016/0003-2697(71)90370-8.

Ben Ali, S., Ferretti, V., Del Bianco, L., Spizzo, F., Belhouchet, M., 2020. Structural, vibrational, optical properties and theoretical studies of a new organic-inorganic material: Tris-acetoguanaminium hexachlorobismuthate monohydrate. J. Mol. Struct. 1199,. https://doi.org/10.1016/j.molstruc.2019.126986 126986.

Ben Salah, A.M., Naïli, H., Arczyński, M., Fitta, M., 2016. 0D and 1D copper(II) coordination polymers based on 2-methyl-1H-imidazole: Structural, vibrational and magnetic characterizations. J. Organomet. Chem. 805, 42–48. https://doi.org/10.1016/j.jorganchem.2016.01.010.

Coronado, E., Day, P., 2004. Magnetic Molecular Conductors. Chem. Rev. 104, 5419–5448. https://doi.org/10.1021/CR030641N.

Derbel, M.A., Jlassi, R., Roisnel, T., Badraoui, R., Krayem, N., Al-Ghulikah, H., Rekik, W., Naïli, H., 2022. The effect of partial substitution of chloride by bromide in the 0-D hybrid material $(C_4H_{12}N_2)[CuCl_4]\cdot 2H_2O$: Structural, vibrational, thermal, *in silico* and . . .and biological characterizations. J. Coord. Chem. 75 (19–24), 2628–2645. https://doi.org/10.1080/00958972.2022.2157722.

Díaz-Requejo, M.M., Pérez, P.J., 2008. Coinage Metal-Catalyzed C−H Bond Functionalization of Hydrocarbons. Chem. Rev. 108, 3379–3394. https://doi.org/10.1021/cr078364y.

Draper, H.H., Hadley, M., 1990. Malondialdehyde determination as index of lipid Peroxidation. Meth. Enzymol. 186, 421–431. https://doi.org/10.1016/0076-6879(90)86135-I.

Flohé, L., Günzler, W.A., 1984. Assays of glutathione peroxidase. Meth. Enzymol. 105, 114–120. https://doi.org/10.1016/S0076-6879(84)05015-1.

Gallati, C.M., Goetzfried, S.K., Ortmeier, A., Sagasser, J., Wurst, K., Hermann, M., Baecker, D., Kircher, B., Gust, R., 2021. Synthesis, characterization and biological activity of bis[3-ethyl-4-aryl-5-(2-methoxypyridin-5-yl)-1-propyl-1,3-dihydro-2H-imidazol-2-ylidene]gold(i) complexes. Dalton Trans. 50 (12), 4270–4279. https://doi.org/10.1039/d0dt03902k.

Gamez, P., Aubel, P.G., Driessen, W.L., Reedijk, J., 2001. Homogeneous bio-inspired copper-catalyzed oxidation reactions. Chem. Soc. Rev. 30, 376–385. https://doi.org/10.1039/b104827a.

Gerçek, Z., Yıldız, U., Ulukaya, E., Akar, R.O., 2022. Synthesis, DNA Binding and Cytotoxic Activity of New copper(II) Complexes of Trisubstituted Imidazoles. Pharm. Chem. J. 55, 1320–1328. https://doi.org/10.1007/s11094-022-02578-2.

Hchicha, K., Korb, M., Badraoui, R., Naïli, H., 2021. A novel sulfate-bridged binuclear copper(II) complex: structure, optical, ADMET and in vivo approach in a murine model of bone metastasis. New J. Chem. 45, 13775–13784. https://doi.org/10.1039/D1NJ02388H.

Henkel, G., Krebs, B., 2004. Metallothioneins: Zinc, Cadmium, Mercury, and Copper Thiolates and Selenolates Mimicking Protein Active Site Features – Structural Aspects and Biological Implications. Chem. Rev. 104, 801–824. https://doi.org/10.1021/CR020620D.

Hfidhi, N., Korb, M., Fitta, M., Čižmár, E., Lang, H., Naïli, H., 2019. Magneto-electronic properties and structural features of unusual bis(μ-aqua) bis(μ-sulfato) bridges in binuclear cobalt-based 4-aminopyridine. Inorg. Chim. Acta 484, 206–213. https://doi.org/10.1016/J.ICA.2018.09.033.

Hfidhi, N., Krayem, N., Erwann, J., Bataille, T., Naïli, H., 2021. Lamellar and Supramolecular Feature of New Tutton's Salts Incorporating 2-Amino-4-Methylpyrimidine: Thermal Stability, Optic Study, Antioxidant and Antimicrobial Activities. J. Inorg. Organomet. Polym. Mater. 31, 1549–1564. https://doi.org/10.1007/s10904-020-01817-x.

Inci, T., Kahraman, E., Goker, E., 2021. Sequential usage of imidazole followed by tamoxifen to enhance the anticancer effect of tamoxifen in estrogen receptor-positive breast cancer cell lines. J. Clin. Oncol. 39, e15057–e. https://doi.org/10.1200/JCO.2021.39.15_-suppl.e15057.

Jiang, Y., Huo, Z., Qi, X., Zuo, T., Wu, Z., 2022. Copper-induced tumor cell death mechanisms and antitumor theragnostic applications of copper complexes. Nanomed. J. 17, 303–324. https://doi.org/10.2217/NNM-2021-0374.

Kayali, R., Çakatay, U., Akçay, T., Altuğ, T., 2006. Effect of alpha-lipoic acid supplementation on markers of protein oxidation in post-mitotic tissues of ageing rat. Cell Biochem. Funct. 24, 79–85. https://doi.org/10.1002/CBF.1190.

Khan, M.S., Hayat, M.U., Khanam, M., Saeed, H., Owais, M., Khalid, M., Shahid, M., Ahmad, M., 2020. Role of biologically important imidazole moiety on the antimicrobial and anticancer activity of Fe(III) and Mn(II) complexes. J. Biomol. Struct. Dyn. 39, 4037–4050. https://doi.org/10.1080/07391102.2020.1776156.

Kirillov, A.M., Kirillova, M.V., Pombeiro, A.J.L., 2012. Multicopper complexes and coordination polymers for mild oxidative functionalization of alkanes. Coordination Chem. Rev. 256, 2741–2759. https://doi.org/10.1016/J.CCR.2012.07.022.

Krushna, C., Mohapatra, C., Dash, K.C., 1977. 4-, 5- and 6-coordinate complexes of copper(II) with substituted imidazoles. J. Inorg. Nucl. chem. 39, 1253–1258. https://doi.org/10.1016/0022-1902(77)80363-1.

Kumar, N., Goel, N., 2022. Recent development of imidazole derivatives as potential anticancer agents. Phys. Sci. Rev. https://doi.org/10.1515/psr-2021-0041.

Kumar, V., Kundu, A., Singh, M., Ramanujachary, K.V., Ramanan, A., 2014. Design of non-molecular coordination solids from aqueous solution: [$CuIIL_nX(H_2O)$], where X = SO_4, Cl or H_2O and L = pyrazole, imidazole or glutamic acid and n = 1 or 4. J. Chem. Sci. 126, 1433–1442. https://doi.org/10.1007/s12039-014-0678-9.

Maryott, A., Smith, E., 1951. Table of Dielectric Constants of Pure Liquids. US Government Printing Office.

Mhadhbi, N., Issaoui, N., Hamadou, W.S., Alam, J.M., Elhadi, A.S., Adnan, M., Badraoui, R., 2022. Physico-Chemical Properties, Pharmacokinetics, Molecular Docking and In-Vitro Pharmacological Study of a Cobalt (II) Complex Based on 2-Aminopyridine. ChemistrySelect 7 (3), e202103592.

Mzid, M., Badraoui, R., Khedir, S.B., Sahnoun, Z., Rebai, T., 2017. Protective effect of ethanolic extract of Urtica urens L. against the toxicity of imidacloprid on bone remodeling in rats and antioxidant activities. Biomed. Pharmacother. 91, 1022–1041.

Naïli, H., Hajlaoui, F., Mhiri, T., Mac Leod, T.C.O., Kopylovich, M. N., Mahmudov, K.T., Pombeiro, A.J.L., 2013. 2-Dihydromethylpiperazinediium-MII (MII = Cu II, FeII, CoII, ZnII) double sulfates and their catalytic activity in diastereoselective nitroaldol (Henry) reaction. Dalton Trans. 42, 399–406. https://doi.org/10.1039/c2dt31300f.

Nyangoga, H., Blouin, S., Libouban, H., Baslé, M.F., Chappard, D., 2010. A single pretreatment by zoledronic acid converts metastases from osteolytic to osteoblastic in the rat. Microsc. Res. Tech. 73, 733–740. https://doi.org/10.1002/JEMT.20814.

Papatriantafyllopoulou, C., Efthymiou, C.G., Raptopoulou, C.P., Terzis, A., Manessi-Zoupa, E., Perlepes, S.P., 2008. Mononuclear versus dinuclear complex formation in nickel(II) sulfate/phenyl(2-pyridyl)ketone oxime chemistry depending on the ligand to metal reaction ratio: Synthetic, spectral and structural studies. Spectrochim. Acta A Mol. Biomol. Spectrosc. 70, 718–728. https://doi.org/10.1016/J.SAA.2007.08.020.

Rayati, S., Khodaei, E., Jafarian, M., Wojtczak, A., 2017. Mn-Schiff base complex supported on magnetic nanoparticles: Synthesis, crystal structure, electrochemical properties and catalytic activities for oxidation of olefins and sulfides. Polyhedron 133, 327–335. https://doi.org/10.1016/J.POLY.2017.05.049.

Sayer, I., Dege, N., Ghalla, H., Moliterni, A., Naïli, H., 2021. Crystal structure, DFT studies and thermal characterization of new luminescent stannate (IV) based inorganic-organic hybrid compound. J. Mol. Struct. 1244,. https://doi.org/10.1016/J.MOLSTRUC.2020.129266 129266.

Sharma, A., Kumar, V., Kharb, R., Kumar, S., Sharma, P.C., Pathak, D.P., 2016. Imidazole Derivatives as Potential Therapeutic Agents. Curr. Pharm. Des. 22 (21), 3265–3301. https://doi.org/10.2174/1381612822666160226144333.

Sharples, J.W., Collison, D., 2014. The coordination chemistry and magnetism of some 3d–4f and 4f amino-polyalcohol compounds. Coord. Chem. Rev. 260, 1–20. https://doi.org/10.1016/J.CCR.2013.09.011.

Sheldrick, G.M., 1996. SADABS, Program for area detector adsorption correction. University of Göttingen, Germany, p. 33.

Solomon, E.I., Szilagyi, R.K., DeBeer George, S., Basumallick, L., 2004. Electronic Structures of Metal Sites in Proteins and Models: Contributions to Function in Blue Copper Proteins. Chem. Rev. 104, 419–458. https://doi.org/10.1021/CR0206317.

Tatara, W., Wójcik, M.J., Lindgren, J., Probst, M., 2003. Theoretical Study of Structures, Energies, and Vibrational Spectra of the Imidazole−Imidazolium System. J. Phys. Chem. 107, 7827–7831. https://doi.org/10.1021/JP030065Z.

Verma, A., Joshi, S., Singh, D., 2013. Imidazole: Having versatile biological activities. J. Inst. Eng. (India): B 94, 1–12. https://doi.org/10.1155/2013/329412.

J.H. Waterborg, The Lowry Method for Protein Quantitation, Humana Press, Totowa, NJ, 2009, pp. 7–10. https://doi.org/10.1007/978-1-59745-198-7_2.

Yahyaoui, S., Rekik, W., Naïli, H., Mhiri, T., Bataille, T., 2007. Synthesis, crystal structures, phase transition characterization and thermal decomposition of a new dabcodiium hexaaquairon (II) bis(sulfate):($C_6H_{14}N_2$). J. Solid State Chem. 180, 3560–3570. https://doi.org/10.1016/j.jssc.2007.10.019.

Yasir Khan, H., Tarique Zeyad, M., Akhter, S., Tabassum, S., Arjmand, F., 2022. Comprehensive structural single crystal X-ray diffraction, spectroscopic & DFT computational simulation and biological in vitro DNA binding & antibacterial studies of polymeric copper(II)-based imidazole drug entity. Inorg. Chim. Acta. 538,. https://doi.org/10.1016/J.ICA.2022.120978 120978.

Mhadhbi, N., Dgachi, S., Ben Ahmed, S., Issaoui, N., Nasr, S., R Badraoui, R., Badraoui, B., Naïli, H., 2023. Vibrational Spectroscopies, Global Reactivity, Molecular Docking, Thermodynamic Properties and Linear and Nonlinear Optical Parameters of Monohydrate Arsonate Salt of 4-Aminopyridine. Chem. Afr. 2023. doi: 10.1007/s42250-023-00620-8.